

Event-Based Motion Magnification

Yutian Chen^{1,2}, Shi Guo^{1,†}, Fangzheng Yu^{1,2}, Feng Zhang¹, Jinwei Gu³ and Tianfan Xue³
¹Shanghai AI Laboratory, ²Zhejiang University, ³The Chinese University of Hong Kong
 {ytchen10, 22130037}@zju.edu.cn, {guoshi, zhangfeng}@pjlab.org.cn,
 {jwgu@cse, tfxue@ie}.cuhk.edu.hk

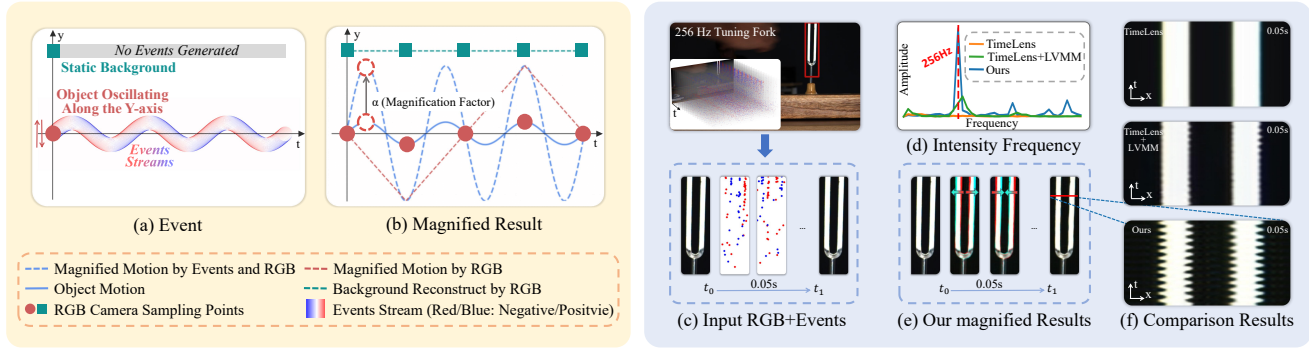


Figure 1. **(Left)** An example of a circular object oscillating along the y-axis shows that event cameras and conventional cameras offer complementary information for high-frequency motion magnification. Event cameras provide temporally-dense data, which help calculate magnified motion (blue dashed line) and solve spectral aliasing (red dashed line) due to the conventional camera’s lower Nyquist frequency relative to motion frequency (blue solid line). However, when relying solely on event cues, reconstructing static backgrounds and non-edge-moving regions becomes challenging due to the absence of event signal. Consequently, the integration of RGB images becomes essential to address this limitation. **(Right)** The magnified result of the real capture video. Our proposed model can effectively magnify the motions at the correct frequencies compared to other solutions. For better visualization of the tuning fork’s motion, we denote different pixels between different frames using red and cyan respectively in (e). **Please refer to the supplementary videos for better visualization of magnification results.**

Abstract

Detecting and magnifying imperceptible high-frequency motions in real-world scenarios has substantial implications for industrial and medical applications. These motions are characterized by small amplitudes and high frequencies. Traditional motion magnification methods rely on costly high-speed cameras or active light sources, which limit the scope of their applications. In this work, we propose a dual-camera system consisting of an event camera and a conventional RGB camera for video motion magnification, containing temporally-dense information from the event stream and spatially-dense data from the RGB images. This innovative combination enables a broad and cost-effective amplification of high-frequency motions. By revisiting the physical camera model, we observe that estimating motion direction and magnitude necessitates the

integration of event streams with additional image features. On this basis, we propose a novel deep network for event-based video motion magnification that addresses two primary challenges: firstly, the high frequency of motion induces a large number of interpolated frames (up to 80), which our network mitigates with a Second-order Recurrent Propagation module for better handling of long-term frame interpolations; and secondly, magnifying subtle motions is sensitive to noise, which we address by utilizing a temporal filter to amplify motion at specific frequencies and reduce noise impact. We demonstrate the effectiveness and accuracy of our dual-camera system and network through extensive experiments in magnifying small-amplitude, high-frequency motions, offering a cost-effective and flexible solution for motion detection and magnification. Project website: <https://openimaginglab.github.io/emm/>.

[†]Corresponding author.

1. Introduction

In the real world, numerous small motions often escape human perception but hold significant implications for industrial and medical applications. These motions are characterized by small amplitudes ranging from micrometers to meters, and high frequencies spanning from a few Hz to MHz. Motion magnification technology facilitates the visualization of these imperceptible motions, thus enabling us to detect object vibrations [21, 23], remotely measure an individual’s vital signs [38], and analyze the physical properties of materials [4, 6, 8]. Such capabilities open doors to a wide array of practical applications.

In high-frequency small motion magnification, spectral aliasing occurs if the camera system’s Nyquist frequency is lower than the motion’s highest inherent frequency. This limitation makes conventional camera systems impractical for such applications (see the red dashed line in Fig. 1 (b)). Therefore, previous image-based motion magnification methods [21, 23, 28, 34, 35, 37, 38, 40] have traditionally relied upon specialized high-speed cameras. However, these high-speed cameras are characterized by their high cost, substantial memory requirements, and limited spatial resolution. In response to the constraints posed by high-speed cameras, Sheinin *et al.* [27] introduced a dual-shutter system. Nevertheless, this method necessitates an active light source and is primarily suited for motion detection within a restricted region, thus constraining its applicability. Therefore, efficiently and conveniently detecting and magnifying low-amplitude high-frequency motion is still challenging.

To overcome temporal frequency constraints, we introduce a dual-camera system comprising an event camera and a conventional RGB camera. Event cameras [5, 26] are neuromorphic sensors designed to only record significant pixel-wise brightness changes. They can record event streams with remarkable temporal precision, often operating at the microsecond level. Unlike high-speed cameras, these brightness-change events are spatially sparse, and thus high-speed recording does not introduce substantial data transmission overhead, making event cameras both cheap and efficient for recording high-speed motion. This is particularly advantageous for motion magnification, where very few pixel changes occur in the presence of small motion, resulting in even sparser events. The information of static pixels is then provided by conventional cameras as complementary information. As shown in Fig. 1 (a) and (b), event cameras provide temporally-dense information, whereas conventional cameras provide spatially-dense data. Consequently, our dual-camera system excels in capturing and amplifying non-linear high-frequency motions.

To solve the motion magnification problem using our dual camera system, we initially revisit their physical camera model and derive an explicit form for the solution. The

solution reveals that the event stream alone is insufficient for determining motion direction and magnitude, and additional image features are required. Based on the key observation that tiny motion is determined by both local RGB image features and polarities of event streams, we propose a novel deep network (as shown in Fig. 2) for event-based video motion magnification, consisting of 1) an encoder that extracts texture, shape and motion representations from low-frame-rate RGB images and corresponding event streams, 2) a manipulator that amplifies the motion, and 3) a decoder that reconstructs high-frame-rate, motion-magnified RGB videos.

Even with the design above, a robust dual-camera magnification network still faces two challenges. First, for every pair of adjacent image frames, we normally need to interpolate more frames than the traditional interpolation networks can handle. For example, to magnify a 512Hz motion with a 20Hz camera, 50-frame interpolation is required, but traditional networks typically handle 15 frames [31–33] or fewer. To tackle this, we augment the Recurrent Neural Network (RNN) with a Second-order Recurrent Propagation (SRP) strategy. By transitioning first-order relationship [24] in RNN to the second order [7, 29], our SRP is adept at handling long-term frame interpolations, meeting the requirements of dual-camera magnification.

Second, the event stream is known to be sensitive to noise [12, 16, 25], and subtle motions make the signal-to-noise ratio even worse. To address this issue, we apply a temporal filter [23, 34] to the motion representation at the test phase and amplify motion at specific frequencies. Through extensive experiments, our dual-camera system and the proposed network demonstrate their effectiveness and accuracy in magnifying real-world small-amplitude, high-frequency motions, as shown in Fig. 1 (f).

In summary, our contributions are as follows:

1. To the best of our knowledge, for the first time, we constructed a dual-camera system comprising both an event camera and a conventional RGB camera for video motion magnification. This system enables a broad and cost-effective amplification of high-frequency motions.
2. We introduce a novel network for the task of event-based video motion magnification, where the second-order recurrent propagation module is designed to better process long term information, and the temporal filter is used to handle the noises from event cameras.

2. Related Work

2.1. Video Motion Magnification

To detect and magnify high-frequency motion, previous video motion magnification methods [21, 23, 34, 35, 38, 40] have primarily relied on expensive 2D RGB high-speed cameras. These methods can be categorized into two

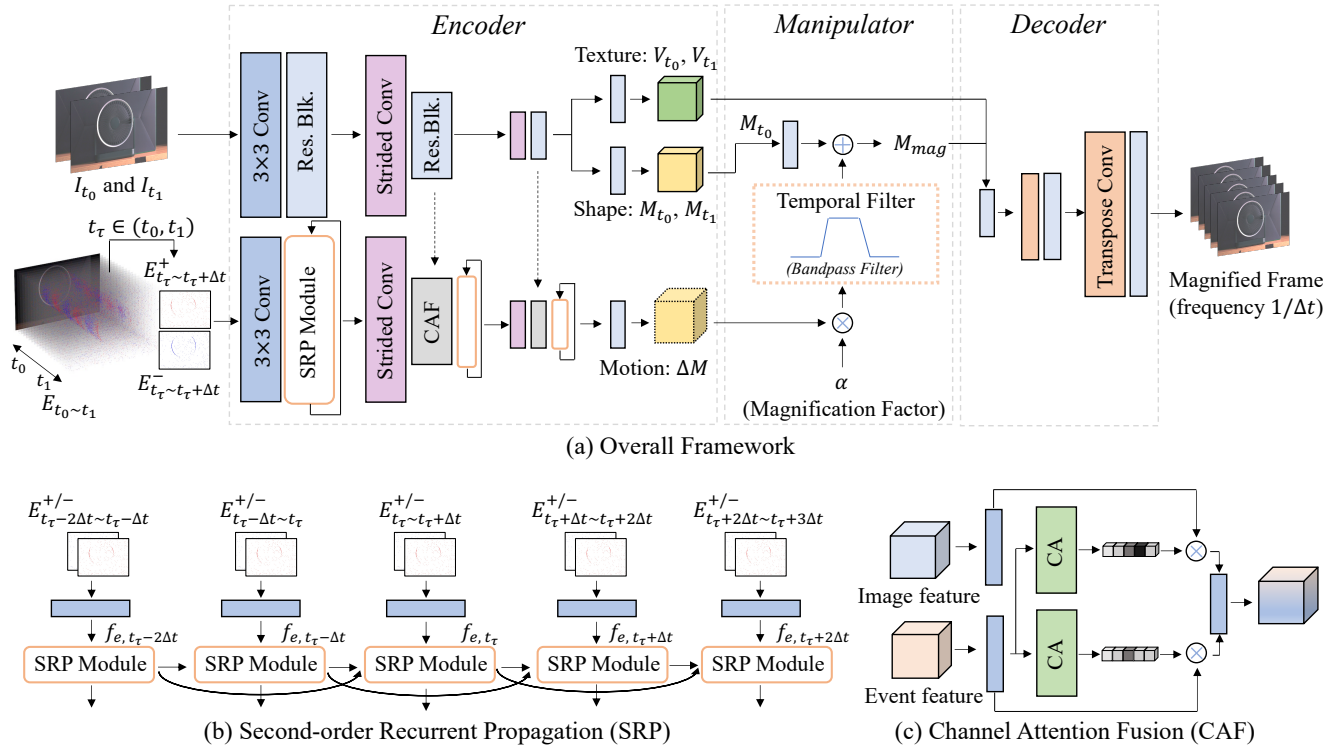


Figure 2. **Illustration of the framework of our network.** The network is designed to utilize RGB images I_{t_0} and I_{t_1} at time t_0 and t_1 to generate high frame rate magnified frames. (a) is the overall framework, which consists of three main components: Encoder, Manipulator, and Decoder. The Encoder extracts temporal-invariant texture V_{t_0} and V_{t_1} , shape M and motion ΔM from RGB and event data. Within it, we introduce a Second-order Recurrent Propagation (SRP) module for optimal long-term event signal processing. We unfold the SRP process across the temporal dimension in (b). Also a Channel Attention Fusion (CAF) module is used for RGB and event data integration. The detail of the CAF module is shown in (c), where ‘CA’ stands for channel attention [3, 15, 39]. The Manipulator linearly magnifies the motion using factor α , producing the magnified motion M_{mag} . To amplify motion at specific frequencies and reduce noise interference, a temporal filter is employed during inference. The Decoder then reconstructs motion-magnified frames leveraging M_{mag} and texture data.

main groups: Lagrangian-based and Eulerian-based approaches. Lagrangian methods [21] explicitly estimate motion and warp video frames based on magnified velocity vectors. However, motion estimation in such methods is challenging and computationally demanding, often leading to visible errors in the results. In contrast, Eulerian approaches [23, 34, 35, 38, 40] decompose video frames into representations using Laplacian pyramids [38], complex steerable pyramid [34, 35] and deep network [23], and then amplify temporal variations at each pixel to magnify motion. However, the 2D RGB high-speed cameras are very expensive, bulky, require extensive data storage capacity, and have lower spatial resolution. To address the limitations associated with high-speed cameras, Sheinin *et al.* [27] introduced a dual-shutter system that employs two standard cameras (60 and 134 Hz) to capture high-frequency motion, reaching frequencies of up to 63 kHz. This approach leverages a rolling shutter sensor for high-speed 1D motion capture and a global rolling shutter sensor to recover high-frequency 2D shifts within the rows of the rolling shut-

ter sensor. However, this method relies on an active light source, which imposes constraints on its application scenarios. To overcome the limitations of previous methods, we utilize the dual camera with the temporally-dense event signals and the spatially-dense RGB images to cost-effectively magnify high-frequency motion.

2.2. Event-based High-speed Scene Imaging

Event cameras [5, 26] represent a novel class of neuromorphic sensors that asynchronously obtain per-pixel intensity changes whenever the logarithmic change in latent irradiance exceeds a preset threshold. In contrast to RGB cameras, event cameras offer several advantages, including high temporal resolution, and ultra-low latency on the order of microseconds, which makes event cameras particularly well-suited for supporting high-speed imaging applications, such as frame interpolation. By leveraging event signals to interpolate high-speed scenes from low-frame-rates RGB videos, Tulyakov *et al.* [32] introduced the Time-Lens framework by combining synthesis-based and flow-

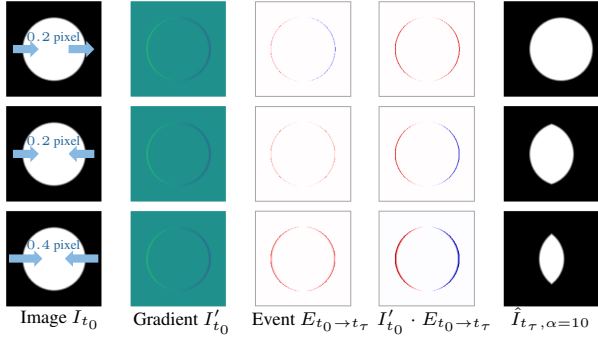


Figure 3. A toy example of 1-D sub-pixel motions of a circular object, demonstrating the connection between images I_{t_0} (and its gradients I'_{t_0}), aggregated events $E_{t_0 \rightarrow t_\tau}$ (blue positive, red negative), and magnified motion $\hat{I}_{t_\tau, \alpha=10}$. We can observe that event polarity itself cannot indicate the motion direction, as the left side and right side of the circular object in the first row move to the same direction, but generate events of different polarities (column 3). However, the multiplication of image gradient and event polarity (column 4, denoted as $I'_{t_0} \cdot E_{t_0 \rightarrow t_\tau}$) actually correlates with the motion direction. Because on both sides, the multiplication is of the same polarity, and the object is also moving in the same direction. In addition, the third row illustrates a scenario where the image gradients and motion direction are consistent with the second row, but the displacement increases from 0.2 to 0.4. This results in a larger number of generated events compared to the second row, hence amplifying the perceived magnitude of motion.

based methods. Building upon this, TimeLens++ [33] enhances the framework with multi-scale feature-level fusion and computes one-shot non-linear inter-frame motion estimation. To fully explore the potential of event cameras, He *et al.* [14] introduced the TimeReplayer, which eliminates the need for high-speed training data by employing an unsupervised cycle-consistent strategy. Additionally, RE-FID [31] acknowledges that input low-frame-rate videos may suffer from blur and proposes a bidirectional recurrent network to jointly address interpolation and deblurring.

However, previous interpolation methods [14, 31–33] typically consider interpolating 3~15 frames, which is much lower than motion magnification task. Our task requires interpolating up to 80 frames for high-frequency motion. Thus we propose a Second-order Recurrent Propagation module to address the challenge of long-term information modeling.

3. Method

3.1. Problem Formulation

Event representation: Event cameras measure brightness changes as an asynchronous stream of events. Each event is triggered when the intensity change is larger than a contrast threshold c . Each event e_i consists of (\mathbf{u}_i, t_i, p_i) , where $\mathbf{u}_i = (x_i, y_i)$ are the pixel coordinates and t_i is the times-

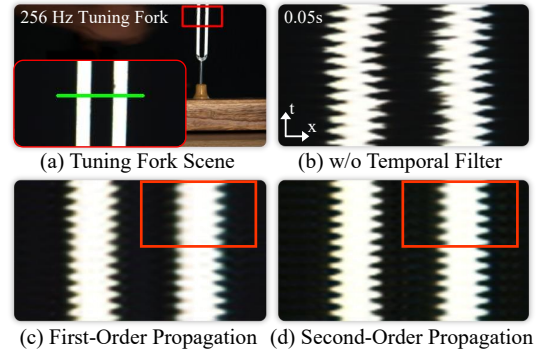


Figure 4. Comparison of Non-Filtering vs. Filtering and First-order Propagation vs. Second-order Propagation.

tamp. The event polarity p_i can be expressed as:

$$p_i = \begin{cases} 1, & \text{if } \log\left(\frac{I(\mathbf{u}_i, t_i)}{I(\mathbf{u}_i, t_i - \delta t)}\right) \geq c(\mathbf{u}_i), \\ -1, & \text{if } \log\left(\frac{I(\mathbf{u}_i, t_i)}{I(\mathbf{u}_i, t_i - \delta t)}\right) \leq -c(\mathbf{u}_i), \\ 0, & \text{otherwise,} \end{cases} \quad (1)$$

where $I(\mathbf{u}_i, t_i)$ is the image intensity at time t_i in location \mathbf{u}_i , $c(\mathbf{u}_i)$ is the spatially-varying threshold, δt is the time interval since the last event occurred at \mathbf{u}_i .

Event-based video motion magnification: The input of our task is two RGB frames I_{t_0} and I_{t_1} at timestamp t_0 and t_1 , the corresponding asynchronous events $\{e_i = (\mathbf{u}_i, t_i, p_i)\}_{i=t_0}^{t_1}$ and the magnification factor α . Our goal is to visualize and magnify the high-frequency motion between t_0 and t_1 , and obtain the motion magnified frames $\{\hat{I}_i\}_{i=t_0}^{t_1}$. The number of interpolation frames \hat{I} can be customized based on the motion frequency.

To solve the above problem, we derive the formula for motion amplification using low-frame-rate images and corresponding events. Following [23, 34], the interpolated unmagnified frame I_{t_τ} can be expressed as:

$$I(\mathbf{u}, t_\tau) = I(\mathbf{u} - \delta(\mathbf{u}, t_0 \rightarrow t_\tau), t_0), \quad (2)$$

where $\delta(\mathbf{u}, t_0 \rightarrow t_\tau)$ represents the motion field (or optical flow) from frame $I(\mathbf{u}, t_0)$ to $I(\mathbf{u}, t_\tau)$.

Under the assumption that the motion vector is small and brightness remains constant, we can use the first-order Taylor expansion to approximate Eq. (2) as:

$$I(\mathbf{u}, t_\tau) \approx I(\mathbf{u}, t_0) - I'(\mathbf{u}, t_0)\delta(\mathbf{u}, t_0 \rightarrow t_\tau), \quad (3)$$

where $I'(\mathbf{u})$ is the image gradient. As the definition of event in Eq. (1), the interpolated frame can be also modeled using event stream by using [18, 20, 30]:

$$I(\mathbf{u}, t_\tau) = I(\mathbf{u}, t_0) \exp\left(c(\mathbf{u}) \int_{t_0}^{t_\tau} p(\mathbf{u}, t) dt\right). \quad (4)$$

Table 1. **Quantitative comparison on synthetic test set.** Our system requires only a small data stream size yet achieves performance comparable to that of LVMM on high-speed video, which requires a data stream 5 times larger.

Method	Data Size (Images + Event)	Images Frame Rate	Uses Events	PSNR	SSIM
LVMM [23] on highspeed video	3.60 M + 0M	900Hz	✗	22.30	0.7309
SuperSloMo [17] + LVMM [23]	0.23 M + 0 M	30Hz	✗	14.32	0.3871
TimeLens [32] + LVMM [23]	0.23 M + 0.49 M	30Hz	✓	17.60	0.5582
Ours	0.23 M + 0.49 M	30Hz	✓	22.32	0.8753

Thus the motion field $\delta(\mathbf{u}, t_0 \rightarrow t_\tau)$ can be obtained by solving Eqs. (3) and (4). For better comprehension, we provide a 1D solution as:

$$\delta(\mathbf{u}, t_0 \rightarrow t_\tau) = \frac{\sum_{\mathbf{u} \in P} s(\mathbf{u}) \cdot \left(\int_{t_0}^{t_\tau} p(\mathbf{u}, t) dt \right) \cdot c(\mathbf{u})}{\sum_{\mathbf{u} \in P} s^2(\mathbf{u})}, \quad (5)$$

where $s(\mathbf{u}) = -I'(\mathbf{u}, t_0)/I(\mathbf{u}, t_0)$ and P is a small window centered at \mathbf{u} . Detailed derivations of 1D and 2D motion magnification solutions are provided in the **supplementary material**.

For an intuitive visualization of the relationship between images, events, and motions in Eq. (5), we employ a 1D sub-pixel motion of a circular object as a toy example in Fig. 3. It underscores the necessity of using both image and event information to deduce the direction and magnitude of motion accurately, which is consistent with Eq. (5).

We simplify Eq. (5) into a function using both RGB and Event signal, denoted as:

$$\delta(\mathbf{u}, t_0 \rightarrow t_\tau) = g(I(\mathbf{u}, t_0), \{p(\mathbf{u}, t)\}_{t=t_0}^{t_\tau}). \quad (6)$$

Then the magnified frame \hat{I}_{t_τ} can be expressed as:

$$\begin{aligned} \hat{I}(\mathbf{u}, t_\tau) &= I(\mathbf{u} - (1 + \alpha)\delta(\mathbf{u}, t_0 \rightarrow t_\tau), t_0) \\ &= I(\mathbf{u} - (1 + \alpha)g(I(\mathbf{u}, t_0), \{p(\mathbf{u}, t)\}_{t=t_0}^{t_\tau}), t_0). \end{aligned} \quad (7)$$

One can observe that, in contrast to previous methods [23, 34, 35, 38, 40], instead of relying on high-frame-rate RGB frames, the proposed approach leverages the temporally-dense event stream and spatially-dense image content information for motion estimation, thus obviating the need for expensive high-speed RGB cameras.

3.2. General Architecture

The derivation of Eq. (7) integrates strong assumptions, such as brightness constancy, into the models and the model is susceptible to sensor noise. Therefore, we abstract the physical model in Eq. (7) into an end-to-end neural network to learn abstractions and priors from data, enhancing its adaptability across diverse and complex scenarios. The overview of our network is illustrated in Fig. 2. Inspired by [23, 34], Our network consists of three parts: the encoder for representation extraction, the manipulator for magnifying motion, and the decoder for frame reconstruction.

Encoder: The encoder is comprised of two branches: the image branch and the event branch. The image branch is dedicated to extract texture representation (V_{t_0} and V_{t_1}) and shape representation (M_{t_0} and M_{t_1}) from the RGB images (I_{t_0} and I_{t_1}). The event branch is used to extract motion representation ΔM_{t_τ} between t_0 and any interval time $t_\tau \in (t_0, t_1)$, which is an implicit representation of $\delta(\mathbf{u}, t_0 \rightarrow t_\tau)$ in Eq. (7).

For the image branch, the RGB images are firstly modeled into deep features using $f_t = F_{rgb}(I_t)$, where F_{rgb} consists of strided convolutions and residual blocks. To reduce the effect of noise and save computational cost, the resolution of feature f_t is 1/8 compared with I_t . Then the texture and shape representations are obtained by:

$$V_t = F_v(f_t), \quad M_t = F_m(f_t), \quad (8)$$

where F_v and F_m are two residual blocks. Note that $(M_{t_0} - M_{t_1})$ represents the shape change between two RGB frames.

For the event branch, the events are first converted into a voxel grid to enable neural networks to process [31–33], denoted as $E \in \mathbb{R}^{2n \times H \times W}$, where n is the interpolated frame number. Following [11], we accumulate the events in a small time interval $\Delta t = \frac{(t_1 - t_0)}{n}$ into two distinct voxel grids E^+ and E^- for positive and negative events, respectively. Such a method can prevent filtering out small motion caused by directly accumulating positive and negative events together and retain a more comprehensive set of information.

To capture high-frequency shape changes between t_0 and t_1 , both the event stream and RGB features are employed, as stated in Eq. (5). Different from explicitly extracting the motion field $\delta(\mathbf{u}, t_0 \rightarrow t_\tau)$ as Eq. (5), we follow the Eulerian approaches and extract the features' implicit motion ΔM_{t_τ} using $F_{\Delta M}$, which can be expressed as:

$$\Delta M_{t_\tau} = F_{\Delta M}(f_{rgb}, \{E_k^{+/-}\}_{k=1}^{(t_\tau - t_0)/\Delta t}), \quad (9)$$

where f_{rgb} are the RGB deep features. $F_{\Delta M}$ consists of strided convolutions, residual blocks, channel-attention fusion (CAF) module, and our proposed second-order recurrent propagation (SRP) module. The CAF module is used to adaptively fuse information from two modalities, *i.e.*, f_{rgb} and $E^{+/-}$. Details of the CAF module can be found in Fig. 2 (c) as presented in [31]. The SRP module has been

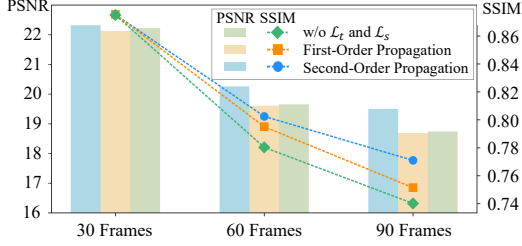


Figure 5. Ablation study of different architectural components.

developed to aggregate information over long-term temporal events. We have observed that this enhancement is particularly beneficial for high-frequency motion magnification. A visualization of the SRP module is presented in Fig. 2 (b), with further details provided in Sec. 3.3.

Manipulator: The manipulator gets the initial shape representation M_{t_0} and motion representation ΔM from the encoder as input, and generates the shape representation of magnified motion.

As the motion representation are expected to be linear to $\delta(\mathbf{u}, t_0 \rightarrow t_\tau)$, we directly multiply magnification factor α to ΔM and add to M_{t_0} extracted from the first images I_{t_0} . For timestamp t_τ , the magnified shape M_{mag, t_τ} is obtained by using:

$$M_{mag, t_\tau} = M_0 + \alpha \Delta M_{t_\tau}. \quad (10)$$

In practical applications, it is often desirable to amplify motion at specific frequencies to reduce noise interference. Therefore, we utilize temporal filters [23, 34] into the manipulator in the inference phase:

$$M_{mag, t_\tau}^{temp} = M_0 + \alpha \Gamma(\Delta M_{t_\tau}), \quad (11)$$

where $\Gamma(\cdot)$ is a 1D temporal filter. This filter is implemented to perform pixel-wise Fourier transformation on per-frame motion presentations ΔM_{t_τ} along the temporal dimension, extract the desired frequency of motion using a band-pass filter, and apply an inverse Fourier transformation to return to the time domain. To evaluate the effect of the temporal filter in our model, we make a comparison on the tuning fork sequence in Fig. 4 (b)(d). It is observable that even in the absence of a temporal filter, our model manages to capture motions at the correct frequencies. The temporal filter further enhances regularity in the motion by effectively decreasing the temporal noise of the event camera.

Decoder: The decoder is designed to reconstruct magnified frames $\{\hat{I}_t\}_{i=t_0}^{t_1}$ using the texture representation V of two frames and magnified shape representation M_{mag} . Finally, at timestamp t_τ , \hat{I}_{t_τ} can be expressed as:

$$\hat{I}_{t_\tau} = F_D(M_{mag, t_\tau}, (V_{t_0} + V_{t_1})/2), \quad (12)$$

where F_D consists of transpose convolutions and residual blocks. Ideally, V_{t_0} and V_{t_1} represent the same information, therefore, for globally invariant texture information, we simply use the average $(V_{t_0} + V_{t_1})/2$.

3.3. Second-order Recurrent Propagation Module

To aggregate temporal event information, there are two typical solutions, *i.e.*, unidirectional recurrent propagation [24] and bidirectional recurrent propagation [31]. Given that the motion we need to amplify ΔM_{t_τ} is computed from t_0 to the current timestamp t_τ , a bidirectional approach is not well-suited to our specific problem. While Recurrent Neural Network (RNN) structures are known for their efficiency, it might not be ideal for our scenario, since our task demands the modeling of distant temporal dependencies due to the insertion of a large number of frames, up to 80 frames. Therefore, we propose a Second-order Recurrent Propagation (SRP) Module.

At time t_τ , the event feature, represented as f_{e, t_τ} , is fused with forward information h_t from the two preceding event frames as:

$$f'_{e, t_\tau}, h_{t_\tau} = F_{SRP}(f_{e, t_\tau}, h_{t_\tau - \Delta t}, h_{t_\tau - 2\Delta t}), \quad (13)$$

where F_{SRP} is the SRP unit. In F_{SRP} , the channel attention [15, 39] is used to adaptive merge event temporal information.

To demonstrate the effectiveness of the SRP module, we compare it with the first-order propagation. The results are shown in Fig. 5 and Fig. 4 (c)(d). The utilization of the SRP module reduces the blurring artifacts of first-order propagation, particularly in scenarios involving a high number of frames for interpolation. Fig. 5 clearly illustrates that the improvement of the model with SRP over the one with normal RNN becomes progressively pronounced as the interpolation sequence lengthens. Both results confirm the SRP's superior performance in the preservation of long-term temporal information.

3.4. Design of Training Loss

Since the texture information extracted from input images I_{t_0} and I_{t_1} should be same, we utilize the texture loss [23]:

$$\mathcal{L}_t = \sqrt{\|V_{t_0} - V_{t_1}\|^2 + \epsilon^2}, \quad (14)$$

where $\sqrt{\|\hat{x} - x\|^2 + \epsilon^2}$ is the Charbonnier penalty function, and ϵ is set to 0.001. We also introduce a shape loss to ensure the consistency between the motions extracted from images and the event:

$$\mathcal{L}_s = \sqrt{\|M_{t_1} - M_{t_0} - \Delta M_{t_1}\|^2 + \epsilon^2}. \quad (15)$$

Then the reconstruction loss is as follows:

$$\mathcal{L}_r = \frac{1}{n} \sum_{k=1}^n \sqrt{\|\hat{I}_{t_0+k\Delta t} - \hat{I}'_{t_0+k\Delta t}\|^2 + \epsilon^2}, \quad (16)$$

where \hat{I}'_t is the ground-truth magnified frame and the interpolated frame number $n = (t_1 - t_0)/\Delta t$. To sum up, the

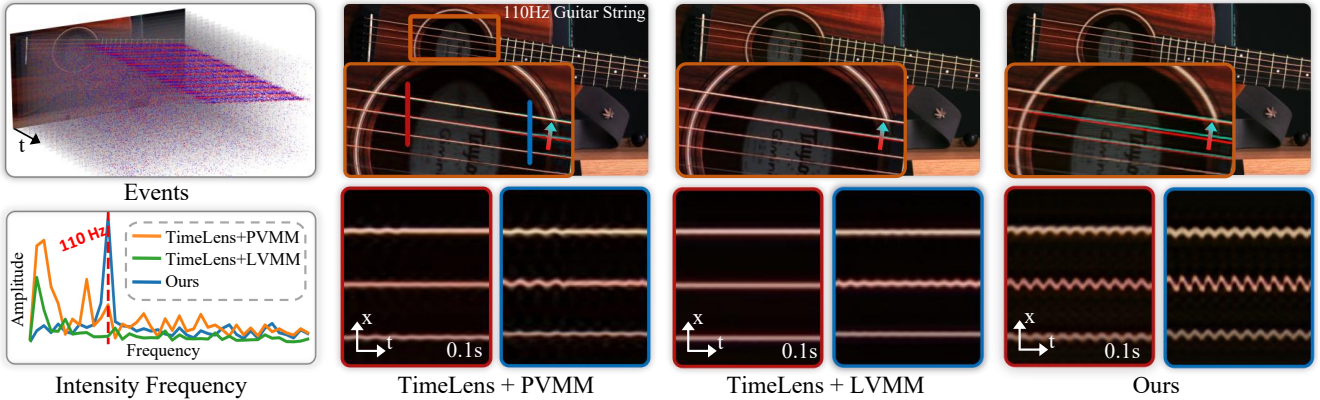


Figure 6. Magnification results of different methods on the real-world video of a 110Hz guitar string.

overall loss to optimize our model is $\mathcal{L} = \mathcal{L}_r + \lambda_1 \mathcal{L}_t + \lambda_2 \mathcal{L}_s$, where λ_1 and λ_2 are trade-off parameters and we set to 0.01 in our experiment.

To evaluate the performance of the loss function, we train a variant without using \mathcal{L}_t and \mathcal{L}_s . The comparison is illustrated in Fig. 5. The inclusion of \mathcal{L}_s and \mathcal{L}_t enhances the network’s performance by improving its ability to utilize long-term event information and discriminate between texture and shape representations. This improvement is particularly evident when interpolating 90 magnified frames.

3.5. Synthetic Training Dataset

Due to the inherent difficulty in acquiring real-world data with small motions, their magnified ground truth, and the corresponding event data, we opt for a simulation-based approach to generate the training dataset. Our simulation pipeline begins with the initial generation of videos containing small-motion and magnified-motion sequences respectively. This is achieved by compositing foreground elements onto a background, where both trajectories and magnification factors are randomly generated. Subsequently, we generate the event data using the event simulator V2E [16].

Following Oh *et al.* [23], we use DIV2K dataset [1, 2] for background and PASCAL VOC dataset [9, 10] for foreground. To handle the magnification of motion with small amplitudes, it is important to simulate sub-pixel motions into our dataset. Therefore, we commence by generating our dataset at a higher resolution, where the motion is more pronounced, and subsequently downsample each frame to the desired resolution. Specifically, we downsample the original 4096×4096 images to 256×256 images, achieving a motion as small as 0.0625 pixels.

After using V2E [16] for simulating event data from downsampled videos, we acquire the training dataset for our task. In the training phase, we utilize the initial and terminal frames of the video in conjunction with the simulated event data as inputs. We employ the magnified video as the

ground-truth data to offer supervision.

4. Experiments

4.1. Training Details

In our experiment, we synthesize a dataset consisting of 10,000 scenes for the training process, each comprising 30 consecutive motion steps. The primary objective of the model is to generate 30 magnified frames from the first and last frames of each scene and the events between them. It is worth noting that due to the utilization of a recurrent framework in $F_{\Delta M}$, our method has the capability to generate randomly interpolated frames, such as 80 frames during our inference phase. Our model is implemented in Pytorch. During training, we use Adam [19] optimizer with an initial learning rate of 1×10^{-4} and weight decay coefficient of 1×10^{-4} for 200k iterations.

4.2. Results on Synthetic Videos

To validate our method’s performance in video motion magnification, we create a synthetic test set with ground truth magnification results. While the test set mirrors the construction method of the training data, it introduces unique foregrounds and backgrounds. It is worth noting that our test set matches the training set of the state-of-the-art RGB video motion magnification method LVMM [23]. Tab. 1 shows our quantitative results. Compared to directly magnify motion in high-speed RGB videos using LVMM, our event-based method presents a notable reduction in data transferring and storage demands (merely $\sim 1/5$ (0.72M/3.60M) of the data volume) but delivers improved outcomes. This suggests that for subtle motions, high-speed cameras might generate excessive data, whereas using event data and low-frame-rate RGB video can produce similarly effective results in a more cost-effective approach. To compare the results using the same low-frame-rate RGB input, we combine LVMM with state-of-the-art interpolation

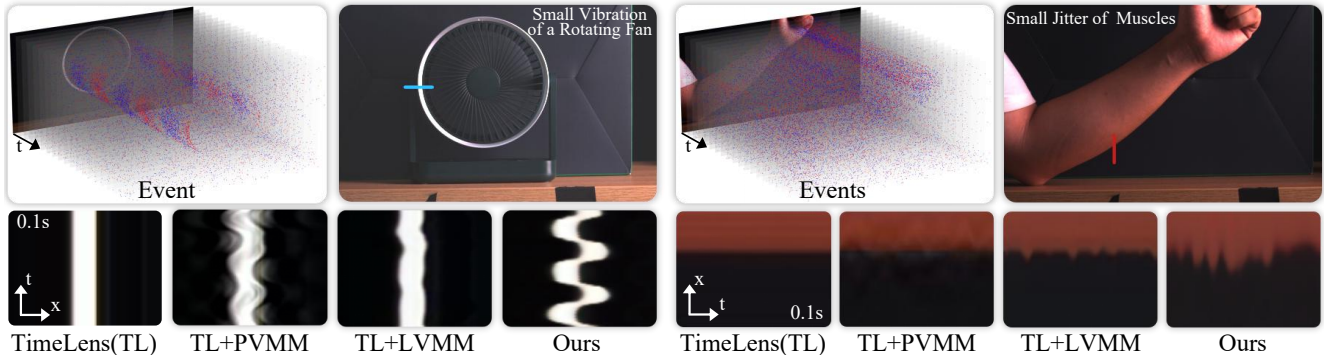


Figure 7. Magnification results of different methods on the real-world video without ground-truth frequency.

methods, *i.e.*, SuperSloMo [17] for RGB-based interpolation and TimeLens [32] for event-based interpolation. The results from SuperSloMo+LVMM are suboptimal due to the linear motion assumptions these algorithms imposed and low sampling rates in the input RGB stream, as illustrated in Fig. 1 (b). Furthermore, compared with TimeLens for event-based frame interpolation followed by LVMM, our method demonstrates an enhancement of approximately 4.7 dB. This gain can be attributed to our end-to-end network, which prevents error accumulation inherent in the two-stage process of interpolation followed by magnification.

4.3. Results on Real-world Video

To validate the effectiveness of our approach in magnifying high-frequency motion in real-world scenarios, we build a RGB-Event dual camera system as Fig. 8. This system consists of a Prophesee EVK4-HD (1280 × 720) event camera and the high-resolution MER2-301-125U3C (2048 × 1536) RGB camera. To ensure alignment between the fields of view from both sensors [13, 36, 41], we implemented a beam splitter positioned in front of the cameras. Both cameras have undergone geometric calibration and temporal synchronization processes. The real-world test set features frame rates of 20 FPS or 10 FPS, with all motions occurring at sub-pixel levels.

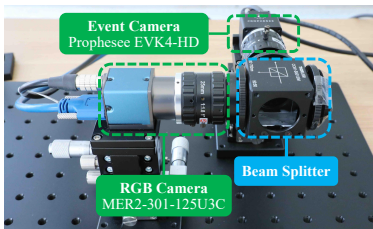


Figure 8. Our RGB-Event dual camera system.

Since currently there is no event-based video motion magnification method publicly available, for a fair comparison, we combine the representative RGB-based motion magnification methods, *i.e.*, PVMM [34] and LVMM [23], with state-of-the-art interpolation methods, TimeLens [32]

for event-based interpolation. The interpolation method is used to increase the frame rate of the input video to avoid spectral aliasing induced by the low sampling rate. We present visual comparisons on real-world datasets featuring ground-truth frequency information, as illustrated in Figs. 1 and 6. The figures depict magnified results from recordings of a 256Hz tuning fork and a 110Hz guitar string, respectively. It is observed that the magnification outputs derived from TimeLens+PVMM and TimeLens+LVMM fall short of representing the inherent motion frequency accurately. Following the application of the temporal filter, only a limited amount of motion can be recovered by TimeLens+PVMM and TimeLens+LVMM. In contrast, our proposed model effectively captures and magnifies the motions at the correct frequencies with precision. We further validate the applicability of our model to various types of motions, including scenarios where ground-truth frequency information is not available. This includes scenarios such as a small vibration of a rotating fan and a small jitter of muscles, which is shown in Fig. 7. Compared to other methods, our approach can magnify motion in a more pronounced and rational manner. **Please refer to our supplementary file for more detailed results on real videos.**

5. Conclusion

In this paper, we addressed the challenges of magnifying high-frequency, small-amplitude motions by introducing a novel dual-camera system that consists of an event camera and a conventional RGB camera. This dual-camera system provides spatially-dense RGB information and temporally-dense event signals, offering advantages in magnifying non-linear high-frequency motions. By using the physic model of events, we provide the analytical solution for event-based motion magnification. From the insight of the solution, we proposed a novel network that effectively manages the inherent challenges in high-frequency motion representation, including interpolation of a large number of frames and the blend of noise with subtle motions. With the introduction of the Second-order Recurrent Propagation strat-

egy, we achieved enhanced long-term temporal information aggregation. Moreover, using the temporal filter for amplifying specific frequency motion heightens the precision of our motion magnification technique. Through experiments, our dual-camera approach, coupled with our proposed network, has proved to be efficient and accuracy in amplifying real-world small-amplitude, high-frequency motions.

References

- [1] Eirikur Agustsson and Radu Timofte. Ntire 2017 challenge on single image super-resolution: Dataset and study. In *IEEE Conf. Comput. Vis. Pattern Recog. Worksh.*, 2017. **7**
- [2] Eirikur Agustsson and Radu Timofte. Ntire 2017 challenge on single image super-resolution: Dataset and study. In *IEEE Conf. Comput. Vis. Pattern Recog. Worksh.*, pages 126–135, 2017. **7**
- [3] Saeed Anwar and Nick Barnes. Real image denoising with feature attention. In *Int. Conf. Comput. Vis.*, pages 3155–3164, 2019. **3**
- [4] Katherine L Bouman, Bei Xiao, Peter Battaglia, and William T Freeman. Estimating the material properties of fabric from video. In *Int. Conf. Comput. Vis.*, pages 1984–1991, 2013. **2**
- [5] Christian Brandli, Raphael Berner, Minhao Yang, Shih-Chii Liu, and Tobi Delbruck. A 240×180 130 db $3 \mu\text{s}$ latency global shutter spatiotemporal vision sensor. *IEEE Journal of Solid-State Circuits*, 49(10):2333–2341, 2014. **2, 3**
- [6] Oral Buyukozturk, Justin G Chen, Neal Wadhwa, Abe Davis, Frédo Durand, and William T Freeman. Smaller than the eye can see: Vibration analysis with video cameras. In *World Conference on Non-Destructive Testing 2016*, 2016. **2**
- [7] Kelvin CK Chan, Shangchen Zhou, Xiangyu Xu, and Chen Change Loy. Basicvsr++: Improving video super-resolution with enhanced propagation and alignment. In *IEEE Conf. Comput. Vis. Pattern Recog.*, pages 5972–5981, 2022. **2**
- [8] Abe Davis, Katherine L Bouman, Justin G Chen, Michael Rubinstein, Frédo Durand, and William T Freeman. Visual vibrometry: Estimating material properties from small motion in video. In *IEEE Conf. Comput. Vis. Pattern Recog.*, pages 5335–5343, 2015. **2**
- [9] M. Everingham, L. Van Gool, C. K. I. Williams, J. Winn, and A. Zisserman. The PASCAL Visual Object Classes Challenge 2010 (VOC2010) Results. <http://www.pascal-network.org/challenges/VOC/voc2010/workshop/index.html>. **7**
- [10] M. Everingham, L. Van Gool, C. K. I. Williams, J. Winn, and A. Zisserman. The PASCAL Visual Object Classes Challenge 2011 (VOC2011) Results. <http://www.pascal-network.org/challenges/VOC/voc2011/workshop/index.html>. **7**
- [11] Daniel Gehrig, Antonio Loquercio, Konstantinos G Derpanis, and Davide Scaramuzza. End-to-end learning of representations for asynchronous event-based data. In *Int. Conf. Comput. Vis.*, pages 5633–5643, 2019. **5**
- [12] Rui Graça, Brian McReynolds, and Tobi Delbruck. Shining light on the dvs pixel: A tutorial and discussion about biasing and optimization. In *IEEE Conf. Comput. Vis. Pattern Recog.*, pages 4044–4052, 2023. **2**
- [13] Jin Han, Chu Zhou, Peiqi Duan, Yehui Tang, Chang Xu, Chao Xu, Tiejun Huang, and Boxin Shi. Neuromorphic camera guided high dynamic range imaging. In *IEEE Conf. Comput. Vis. Pattern Recog.*, pages 1730–1739, 2020. **8**
- [14] Weihua He, Kaichao You, Zhendong Qiao, Xu Jia, Ziyang Zhang, Wenhui Wang, Huchuan Lu, Yaoyuan Wang, and Jianxing Liao. Timereplayer: Unlocking the potential of event cameras for video interpolation. In *IEEE Conf. Comput. Vis. Pattern Recog.*, pages 17804–17813, 2022. **4**
- [15] Jie Hu, Li Shen, and Gang Sun. Squeeze-and-excitation networks. In *IEEE Conf. Comput. Vis. Pattern Recog.*, pages 7132–7141, 2018. **3, 6**
- [16] Yuhuang Hu, Shih-Chii Liu, and Tobi Delbruck. v2e: From video frames to realistic dvs events. In *IEEE Conf. Comput. Vis. Pattern Recog.*, pages 1312–1321, 2021. **2, 7**
- [17] Huaizu Jiang, Deqing Sun, Varun Jampani, Ming-Hsuan Yang, Erik Learned-Miller, and Jan Kautz. Super slo-mo: High quality estimation of multiple intermediate frames for video interpolation. In *IEEE Conf. Comput. Vis. Pattern Recog.*, pages 9000–9008, 2018. **5, 8**
- [18] Zhe Jiang, Yu Zhang, Dongqing Zou, Jimmy Ren, Jiancheng Lv, and Yebin Liu. Learning event-based motion deblurring. In *IEEE Conf. Comput. Vis. Pattern Recog.*, pages 3320–3329, 2020. **4**
- [19] Diederik P. Kingma and Jimmy Ba. Adam: A method for stochastic optimization. *CoRR*, abs/1412.6980, 2014. **7**
- [20] Songnan Lin, Jiawei Zhang, Jinshan Pan, Zhe Jiang, Dongqing Zou, Yongtian Wang, Jing Chen, and Jimmy Ren. Learning event-driven video deblurring and interpolation. In *Eur. Conf. Comput. Vis.*, pages 695–710. Springer, 2020. **4**
- [21] Ce Liu, Antonio Torralba, William T Freeman, Frédo Durand, and Edward H Adelson. Motion magnification. *ACM Trans. Graph.*, 24(3):519–526, 2005. **2, 3**
- [22] Bruce D Lucas and Takeo Kanade. An iterative image registration technique with an application to stereo vision. In *IJCAI*, pages 674–679, 1981. **1**
- [23] Tae-Hyun Oh, Ronnachai Jaroensri, Changil Kim, Mohamed Elgharib, Frédo Durand, William T Freeman, and Wojciech Matusik. Learning-based video motion magnification. In *Eur. Conf. Comput. Vis.*, pages 633–648, 2018. **2, 3, 4, 5, 6, 7, 8, 1**
- [24] Yansong Peng, Yueyi Zhang, Zhiwei Xiong, Xiaoyan Sun, and Feng Wu. Get: Group event transformer for event-based vision. In *Int. Conf. Comput. Vis.*, pages 6038–6048, 2023. **2, 6**
- [25] Antonio Rios-Navarro, Shasha Guo, Abarajithan Gnaneswaran, Keerthivasan Vijayakumar, Alejandro Linares-Barranco, Thea Aarrestad, Ryan Kastner, and Tobi Delbruck. Within-camera multilayer perceptron dvs denoising. In *IEEE Conf. Comput. Vis. Pattern Recog.*, pages 3932–3941, 2023. **2**
- [26] Teresa Serrano-Gotarredona and Bernabé Linares-Barranco. A 128×128 1.5% contrast sensitivity 0.9% fpn $3 \mu\text{s}$ latency

- 4 mw asynchronous frame-free dynamic vision sensor using transimpedance preamplifiers. *IEEE Journal of Solid-State Circuits*, 48(3):827–838, 2013. [2](#), [3](#)
- [27] Mark Sheinin, Dorian Chan, Matthew O’Toole, and Srinivasa G Narasimhan. Dual-shutter optical vibration sensing. In *IEEE Conf. Comput. Vis. Pattern Recog.*, pages 16324–16333, 2022. [2](#), [3](#)
- [28] Jasdeep Singh, Subrahmanyam Murala, and G Kosuru. Multi domain learning for motion magnification. In *IEEE Conf. Comput. Vis. Pattern Recog.*, pages 13914–13923, 2023. [2](#)
- [29] Rohollah Soltani and Hui Jiang. Higher order recurrent neural networks. *arXiv preprint arXiv:1605.00064*, 2016. [2](#)
- [30] Lei Sun, Christos Sakaridis, Jingyun Liang, Qi Jiang, Kailun Yang, Peng Sun, Yaozu Ye, Kaiwei Wang, and Luc Van Gool. Event-based fusion for motion deblurring with cross-modal attention. In *Eur. Conf. Comput. Vis.*, pages 412–428. Springer, 2022. [4](#)
- [31] Lei Sun, Christos Sakaridis, Jingyun Liang, Peng Sun, Jiezhong Cao, Kai Zhang, Qi Jiang, Kaiwei Wang, and Luc Van Gool. Event-based frame interpolation with ad-hoc deblurring. In *IEEE Conf. Comput. Vis. Pattern Recog.*, pages 18043–18052, 2023. [2](#), [4](#), [5](#), [6](#)
- [32] Stepan Tulyakov, Daniel Gehrig, Stamatios Georgoulis, Julius Erbach, Mathias Gehrig, Yuanyou Li, and Davide Scaramuzza. Time lens: Event-based video frame interpolation. In *IEEE Conf. Comput. Vis. Pattern Recog.*, pages 16155–16164, 2021. [3](#), [5](#), [8](#), [1](#)
- [33] Stepan Tulyakov, Alfredo Bochicchio, Daniel Gehrig, Stamatios Georgoulis, Yuanyou Li, and Davide Scaramuzza. Time lens++: Event-based frame interpolation with parametric non-linear flow and multi-scale fusion. In *IEEE Conf. Comput. Vis. Pattern Recog.*, pages 17755–17764, 2022. [2](#), [4](#), [5](#)
- [34] Neal Wadhwa, Michael Rubinstein, Frédo Durand, and William T Freeman. Phase-based video motion processing. *ACM Trans. Graph.*, 32(4):1–10, 2013. [2](#), [3](#), [4](#), [5](#), [6](#), [8](#), [1](#)
- [35] Neal Wadhwa, Michael Rubinstein, Frédo Durand, and William T Freeman. Riesz pyramids for fast phase-based video magnification. In *IEEE Int. Conf. on Comput. Photo.*, pages 1–10. IEEE, 2014. [2](#), [3](#), [5](#)
- [36] Zihao W Wang, Peiqi Duan, Oliver Cossairt, Aggelos Katsaggelos, Tiejun Huang, and Boxin Shi. Joint filtering of intensity images and neuromorphic events for high-resolution noise-robust imaging. In *IEEE Conf. Comput. Vis. Pattern Recog.*, pages 1609–1619, 2020. [8](#)
- [37] Daniel McDuff Weixuan Chen. Deepmag: Source-specific change magnification using gradient ascent. *ACM Trans. Graph.*, 40(2):1–14, 2020. [2](#)
- [38] Hao-Yu Wu, Michael Rubinstein, Eugene Shih, John Guttag, Frédo Durand, and William Freeman. Eulerian video magnification for revealing subtle changes in the world. *ACM Trans. Graph.*, 31(4):1–8, 2012. [2](#), [3](#), [5](#)
- [39] Syed Waqas Zamir, Aditya Arora, Salman Khan, Munawar Hayat, Fahad Shahbaz Khan, Ming-Hsuan Yang, and Ling Shao. Learning enriched features for real image restoration and enhancement. In *Eur. Conf. Comput. Vis.*, pages 492–511. Springer, 2020. [3](#), [6](#)
- [40] Yichao Zhang, Silvia L Pinteá, and Jan C Van Gemert. Video acceleration magnification. In *IEEE Conf. Comput. Vis. Pattern Recog.*, pages 529–537, 2017. [2](#), [3](#), [5](#)
- [41] Chu Zhou, Minggui Teng, Jin Han, Jinxiu Liang, Chao Xu, Gang Cao, and Boxin Shi. Deblurring low-light images with events. *Int. J. Comput. Vis.*, 131(5):1284–1298, 2023. [8](#)

Event-Based Motion Magnification

Supplementary Material

A. Video Comparisons

We present the visual result of Figs. 1, 6 and 7 in the main paper. Due to the characteristic of the problem, we provide supplementary video for better visualization. The video contains video comparisons with Timelens[32]+PVMM[34] and Timelens[32]+LVMM[23]. One can see that our method can well reconstruct rigid body motion with accurate frequency. Additionally, the video shows results at varying magnification factors.

B. Sub-pixel Motion Visualization

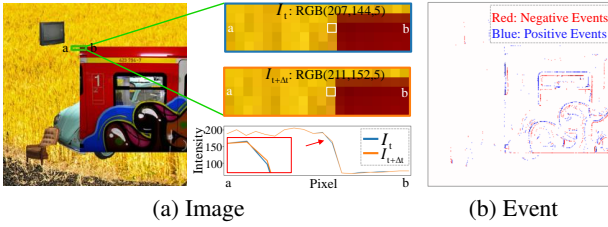


Figure 9. Our synthetic dataset with 0.0625-pixel motions.

In Fig. 9, we visualize sub-pixel motions in our synthetic dataset. It can be observed that the primary manifestation of these sub-pixel motions is in the intensity variations of RGB images. Moreover, the corresponding event signals, generated using the V2E simulator, effectively record these sub-pixel movements.

C. Representation Visualization

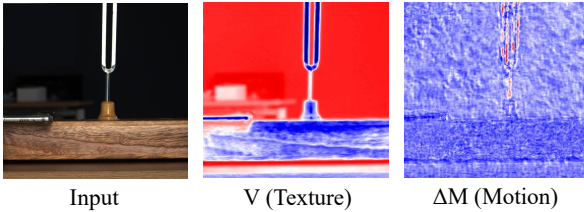


Figure 10. A visualization of texture representation (denoted as V) and motion representation (denoted as ΔM) in the network.

To better interpret our network, we visualize one channel of texture representation and motion representation in our network. As we can see in Fig. 10, the texture representation captures the wood's grain and the background stationary objects while the motion representation mainly captures the moving edges of the tuning fork and the movements of the block supporting the tuning fork. This further

illustrates our encoder's capability to distinguish and extract the texture information and motion information separately.

D. Derivations of Explicit Motion Solution based on Event and RGB

Based on Eqs. (2) and (3) in the main paper, we derive:

$$I(\mathbf{u}) - I'(\mathbf{u})\delta(\mathbf{u}, t_0 \rightarrow t_\tau) = I(\mathbf{u}) \cdot \exp(c(\mathbf{u}) \cdot p(\mathbf{u})), \quad (17)$$

For ease of notation, we only consider motion within a specific time interval, thereby obviating the necessity for the temporal variable. In our description, we denote $\delta(\mathbf{u})$ and $p(\mathbf{u})$ as $\delta(\mathbf{u}, t_0 \rightarrow t_\tau)$ and $\int_{t_0}^{t_\tau} p(\mathbf{u}, t) dt$ respectively. Let us define $s(\mathbf{u})$ as $-I'(\mathbf{u})/I(\mathbf{u})$, and divide $I(\mathbf{u})$ on both sides of the equation above, we get:

$$s(\mathbf{u})\delta(\mathbf{u}, t_0 \rightarrow t_\tau) = \exp(c(\mathbf{u}) \cdot p(\mathbf{u})) - 1 \approx c(\mathbf{u}) \cdot p(\mathbf{u}). \quad (18)$$

1D Solution: Following the Lucas-Kanade method [22], we assume that $\delta(\mathbf{u}, t_0 \rightarrow t_\tau)$ approximately constant within a window P centered at the pixel coordinate \mathbf{u} and $\mathbf{u}_1, \mathbf{u}_2, \dots, \mathbf{u}_n$ are the pixels inside the window. The objective function of Eq. (18) is:

$$\min_{\delta} \|\mathbf{A}\delta(\mathbf{u}) - \mathbf{b}\|^2, \quad (19)$$

where $\mathbf{A} = [s(\mathbf{u}_1) \dots s(\mathbf{u}_n)]^T$ and $\mathbf{b} = [c(\mathbf{u}_1)p(\mathbf{u}_1) \dots c(\mathbf{u}_n)p(\mathbf{u}_n)]^T$. The minimum value is:

$$\delta(\mathbf{u}) = \frac{\sum_{\mathbf{u} \in P} s(\mathbf{u}) \cdot p(\mathbf{u}) \cdot c(\mathbf{u})}{\sum_{\mathbf{u} \in P} s^2(\mathbf{u})}. \quad (20)$$

And recall again, $s(\mathbf{u}) = -I'(\mathbf{u})/I(\mathbf{u})$.

2D Solution: Similarly, we define a window P centered at the pixel coordinate \mathbf{u} . Compare with 1D motion, the image gradient $I'(\mathbf{u})$ and motion $\delta(\mathbf{u})$ becomes 2D vector. Thus, we define $s(\mathbf{u}) = [-I_x(\mathbf{u})/I(\mathbf{u}) \quad -I_y(\mathbf{u})/I(\mathbf{u})] = [s_x(\mathbf{u}) \quad s_y(\mathbf{u})]$, and the objective function is:

$$\min_{\delta} \|\mathbf{A}\delta(\mathbf{u}) + \mathbf{b}\|^2, \quad (21)$$

$$\text{where } \mathbf{A} = \begin{bmatrix} s_x(\mathbf{u}_1) & s_y(\mathbf{u}_1) \\ s_x(\mathbf{u}_2) & s_y(\mathbf{u}_2) \\ \vdots & \vdots \\ s_x(\mathbf{u}_n) & s_y(\mathbf{u}_n) \end{bmatrix}, \mathbf{b} = \begin{bmatrix} c(\mathbf{u}_1)p(\mathbf{u}_1) \\ c(\mathbf{u}_2)p(\mathbf{u}_2) \\ \vdots \\ c(\mathbf{u}_n)p(\mathbf{u}_n) \end{bmatrix},$$

Finally, the minimum value of Eq. (21) is:

$$\begin{aligned} \delta(\mathbf{u}) &= (\mathbf{A}^T \mathbf{A})^{-1} \mathbf{A}^T \mathbf{b} \\ &= \frac{1}{\sum s_x(\mathbf{u})^2 \sum s_y(\mathbf{u})^2 - (\sum s_x(\mathbf{u})s_y(\mathbf{u}))^2} \\ &\quad \begin{bmatrix} \sum s_y(\mathbf{u})^2 \sum SP_x(\mathbf{u}) - \sum s_x(\mathbf{u})s_y(\mathbf{u}) \sum SP_y(\mathbf{u}) \\ - \sum s_x(\mathbf{u})s_y(\mathbf{u}) \sum SP_x(\mathbf{u}) + \sum s_x(\mathbf{u})^2 \sum SP_y(\mathbf{u}) \end{bmatrix}, \end{aligned} \tag{22}$$

where $SP_x(\mathbf{u}) = s_x(\mathbf{u})c(\mathbf{u})p(\mathbf{u})$ and $SP_y(\mathbf{u}) = s_y(\mathbf{u})c(\mathbf{u})p(\mathbf{u})$.